# RSC Advances

ROYAL SOCIETY
OF **CHEMISTRY**

www.rsc.org/advances

1    **Improved Coulombic efficiency and cycleability of SnO$_2$-Cu-Graphite**

2    **composite anode with dual scale embedding structure**

3

4    Bin Lu[a,b], Renzong Hu[a,b], Jiangwen Liu[a,b], Jun Liu[a,b], Hui Wang[a,b,*], Min Zhu[a,b]

5

6    [a] School of Materials Science and Engineering, Key Laboratory of Advanced Energy Storage Materials of

7    Guangdong Province, South China University of Technology, Guangzhou, 510641, China

8    [b] China-Australia Joint Laboratory for Energy & Environmental Materials, South China University of

9    Technology, Guangzhou, 510641, China

10

11    * Corresponding author.

12    Tel.: +86-20-87112762; Fax: +86-20-87111317

13    E-mail address: mehwang@scut.edu.cn (H Wang)

14

15

16

17

18

19

20

21

1   **Abstract**

2       To improve the Coulombic efficiency (CE) and cycle life of $SnO_2$ anode in lithium ion

3   batteries, $SnO_2$-Cu-Graphite composites with dual scale embedding structure are synthesized

4   by ball milling. The $SnO_2$-Cu composite, in which $SnO_2$ nanoparticles with grain size less

5   than 10 nm are uniformly dispersed in inactive nanocrystalline Cu matrix, is firstly obtained

6   by milling the mixture of $SnO_2$ and Cu nanopowders (molar ratio 1:2), and then further mill

7   with graphite (C) to obtain $SnO_2$-Cu-C composite with microsized graphite sheets as matrix

8   of $SnO_2$-Cu composite. The 50h-milled $SnO_2$-Cu composite exhibits higher initial CE

9   ($76.0\pm1.5\%$) and subsequent CE than 50h-milled $SnO_2$. Furthermore, the $SnO_2$-Cu-C

10  composite anode is capable of retaining a maximum charge capacity of 450.8 mAh $g^{-1}$ at 100

11  mA $g^{-1}$ after 80 cycles with a capacity retention ratio of 74.4%, displaying superior cyclic

12  stability to as-milled $SnO_2$, $SnO_2$-Cu and $SnO_2$-C composites. The improved CE and

13  cycleability are attributed to the unique dual scale embedding structure that offers good

14  conductivity of electron and lithium ion as well as the nanostructure stability of active

15  materials. This unique composite structure might be extended to other high-capacity anode

16  materials, to achieve high performance lithium ion batteries.

17

21

1   **1. Introduction**

2   The anode materials with high-energy density and long cycle life is one of keys for the

3   development of lithium-ion batteries.[1-3] $SnO_2$ has been intensively investigated as alternative

4   anode to commercially available graphite because of its high theoretical specific capacity of

5   ~1494 mAh $g^{-1}$, which is four times as that of graphite. The de-/lithiation mechanism of $SnO_2$

6   could be described by the two-step reactions,[4-8] *i.e.,* the conversion reaction ($SnO_2 + 4Li^+ +$

7   $4e^- \leftrightarrow Sn + 2Li_2O$) and alloying reaction ($Sn + xLi^+ + xe^- \leftrightarrow Li_xSn, 0 \leq x \leq 4.4$), which could

8   contribute theoretical capacity of 712 and 782 mAh $g^{-1}$, respectively. However, the

9   reversibility of the conversion reaction of $SnO_2$ is rather poor, resulting in large initial

10  irreversible capacity and low initial Coulombic efficiency (ICE), the theoretical ICE value is

11  only 52.4% if the conversion reaction is fully irreversible.[7-12] In addition, the huge volume

12  variation (~300%) caused by lithium insertion and extraction of Sn results in the loss of active

13  materials and rapid capacity fade, and thus the cyclic CE and reversible capacity are further

14  decreased.[13-15]

15  Extensive research efforts have been devoted to improving the electrochemical

16  performances of $SnO_2$ anode.[7-12, 16-20] Undoubtedly, the nanosizing strategy is the most

17  effective way to improve not only the reversibility of $SnO_2$ but also ease the huge internal

18  stress of Sn particles. It was found that Sn nanoparticles generated from ultrafine $SnO_2$ readily

19  reacted with $Li_2O$ in the charging process, which was verified by the anodic peaks appearing

20  above 1.3V in the cyclic voltammetry curve[7-11] and the TEM observation of SnO and $SnO_2$.[12]

21  Further, constructing nanostructured multiphase composite is shown to greatly improve the

1  ICE and cyclic performance of $SnO_2$ anode simultaneously.[10-12, 17-19] On the composition

2  design of $SnO_2$ based composite, the light-weight carbon matrix is mostly used because of

3  excellent electric conductivity and stress buffering effect.[18-20] For example, Lu *et al.*[10]

4  prepared $SnO_2@C$ composite by *in-situ* hydrolysis method, in which ultrafine $SnO_2$ was

5  encapsulated in ordered tubular mesoporous carbon. The composite electrode showed a

6  considerably high initial reversible capacity of 978 mAh $g^{-1}$ at a current density of 200 mA $g^{-1}$,

7  which even increased up to 1039 mAh $g^{-1}$ after 100 cycles. However, the mechanism of those

8  reported unusual high reversible capacity and Coulombic efficiency has not been fully

9  revealed, and in particular, those synthetic processes usually include complicated steps and

10  offer limited throughput.

11      Recently, conventional milling and plasma-assisted milling techniques have been used to

12  synthesize various Sn-C, $SnO_2$-C composites with specific structure and enhanced

13  electrochemical performances.[21, 22] Nevertheless, the previously reported ICE of $SnO_2$ based

14  anodes prepared by the ball milling is normally low,[21-24] which needs further improvement. It

15  is expected that the transition metals like Cu have the excellent electro-catalytic activity and

16  conductivity, which should facilitate the $Li_2O$ decomposition.[25] Also, the Cu additive is

17  beneficial to not only the dispersion and refinement of $SnO_2$ particles in the milling process

18  but also maintain the nanostructure of $SnO_2$ during cycling, which would promote the

19  conversion and alloying reactions of $SnO_2$.

20      Herein, focusing on the improvement in CE and cyclic stability, the $SnO_2$-Cu composite

21  was designed and prepared by ball milling. We prepared the $SnO_2$-Cu composite through ball

1  milling, aiming to obtain the soft Cu matrix embedded by nanosized $SnO_2$ particles. To

2  further improve the cyclic performance of $SnO_2$-Cu composite, the graphite was added. The

3  relationship between the microstructure and electrochemical performances of the as-milled

4  $SnO_2$-Cu and $SnO_2$-Cu-C composites as well as the dependence on the preparing parameters

5  and the composition were investigated in detail.

6

7  **2. Experimental**

8  **2.1 Materials preparation**

9  The raw materials are commercial natural graphite (99.9%; 38μm; Shanghai Colloid

10  Chemical Plant, China), $SnO_2$ (99.99%, 50~70nm, Aladdin Industrial Inc., China) and Cu

11  (99.9%, 80~100nm, Shanghai ST-nano Tech Co., Ltd., China) nanopowders. Firstly, the $SnO_2$

12  and Cu nanopowders with molar ratio of 1:2 were milled to form the $SnO_2$-Cu composite, the

13  milling was performed on a planetary mill (QM-3SP4, China) with the weight ratio of

14  ball-to-powder of 20:1 at 500 rpm for 10h and 50h, yielding the composites denoted as

15  $SnO_2$-Cu-10h and $SnO_2$-Cu-50h, respectively. For comparison, a manually ground $SnO_2$-Cu

16  mixture was prepared and denoted as $SnO_2$-Cu-0h, and the pure $SnO_2$ was milled for 50h

17  using the same milling parameters and denoted as $SnO_2$-50h. Secondly, the $SnO_2$-Cu-50h

18  composite was further milled with 10, 20, 30 wt.% graphite for 20h at 500rpm with

19  ball-to-powder weight ratio of 30:1, yielding the composites termed as $SnO_2$-Cu-50h-10%C,

20  $SnO_2$-Cu-50h-20%C, $SnO_2$-Cu-50h-30%C, respectively. Similarly, the $SnO_2$-Cu-10h

21  composite and 50h-milled $SnO_2$ were also milled with 30 wt.% graphite for 20h, the resultant

1    composites were termed as $SnO_2$-Cu-10h-30%C and $SnO_2$-50h-30%C, respectively. The

2    graphite was pre-milled for 10h at 500 rpm with the same ball-to-powder weight ratio. To

3    prevent the Cu nanopowders from oxidation, all the powder mixtures were sealed in the

4    stainless steel vial under pure argon atmosphere. After each 30 min of milling, the operation

5    was suspended for 30 min to avoid temperature rising, and the milled powders were collected

6    under pure argon atmosphere without heavy scrapping.

7    **2.2 Materials Characterization and Electrochemical measurement**

8        The X-ray diffractometer (XRD, Philips X'Pert MPD) with Cu-$K_\alpha$ radiation, the field

9    emission scanning electron microscope (SEM, Carl Zeiss supra40) and transmission electron

10   microscope (TEM, JEOL-2100) operating at 200kV were used to characterize the phase

11   structure, morphology and distribution of the composites. The milled $SnO_2$-Cu-10h and

12   $SnO_2$-Cu-50h powders for SEM observation were compacted and followed by polishing

13   process, while the other powder samples were dispersed and directly observed in the SEM

14   experiments. As for the TEM specimen preparation, the powder was transferred out from the

15   Ar-filled glove box and dispersed on a holey carbon film supported by a copper grid very

16   quickly.

17       The electrochemical properties of the as-prepared composites were measured using

18   coin-type half-cells (CR2016) assembled in an Ar-filled glove box with oxygen and moisture

19   content less than 1 ppm. The working electrode was prepared by dissolving 80 wt.% active

20   powders, 10 wt.% conductivity agent (Super-P), and 10 wt.% binder (polyvinylidene fluoride,

21   PVdF) in solvent (N-methyl-2-pyrrolidone, NMP) with appropriate viscosity. Then the slurry

1 was coated onto copper foils by a spin coater and dried at 120°C in a vacuum oven for 10h.

2 The loading of active materials was 1.5~1.8 mg cm$^{-2}$. Lithium metal foils were used as

3 counter and reference electrodes and polyethylene membranes (Teklon@Gold LP) as

4 separators. The electrolyte was LiPF$_6$ (1M) in a mixture of ethylene carbonate/diethyl

5 carbonate/ethyl methyl carbonate (EC/DEC/EMC, 1:1:1, *v/v/v*, Shanshan Tech Co., Ltd.).

6 Galvanostatic charge−discharge measurements were performed with battery testers

7 (CT2001A, Land) at various current densities in the range of 0.01−3.0 V *vs.* Li/Li$^+$, and the

8 current density and capacity were based on the weight of composite materials (such as

9 SnO$_2$-C, SnO$_2$-Cu, SnO$_2$-Cu-C) without conductive agent and binder. Cyclic voltammetry

10 (CV) test over the potential range of 0.0−3.0 V *vs.* Li/Li$^+$ at a scan rate of 0.2 mv s$^{-1}$ was

11 performed on an electrochemical workstation (Interface 1000, Gamry). All the tests were

12 carried out at ambient temperature.

13

14 **3. Results and Discussion**

15 **3.1 SnO$_2$-Cu composites**

16 Fig. 1a shows the XRD patterns of SnO$_2$-Cu composites milled for different times.

17 Comparing with the sharp diffraction peaks in the un-milled SnO$_2$-Cu-0h sample, the peaks of

18 SnO$_2$ and Cu become broadening and weakening with the increasing milling time, indicating

19 the striking grain refinement of SnO$_2$ and Cu by milling. Based on the XRD peak profile

20 analysis using the Scherer equation,[26] the crystallite sizes of SnO$_2$ and Cu after 50h of milling

21 are calculated as ca. 9 nm and 13 nm, respectively. It is observed in the 50-milled composite

1    that a weak Fe(110) reflection appears around 44.6°, which indicates small amount of Fe

2    contamination caused by long time milling. Meanwhile, the Cu(111) peak shifts to the lower

3    angle, which is an indication of the increase in the lattice constant of Cu. This might be owing

4    to the formation of the Cu(Sn) solid solution by milling, because small amount of Sn is

5    possibly formed via the mechanochemical reaction between Cu and $SnO_2$, and its relatively

6    larger atomic radius ($r_{Sn}$=0.158 nm) than Cu ($r_{Cu}$=0.128 nm) results in the lattice expansion of

7    Cu. The influence of the Fe contamination on the electrochemical performance of as-milled

8    composites will be not further discussed due to its little amount.

9       Fig. 1b-e show the SEM images of pristine $SnO_2$, Cu nanopowders and $SnO_2$-Cu

10   composites milled for different times, and Fig. S1 (see the ESI) shows the back-scattered

11   electron SEM image of $SnO_2$-Cu-10h composite. Fig. 1b and Fig. 1c show that the pristine Cu

12   and $SnO_2$ nanopowders have a particle size of 80 ~ 200 nm and 50 ~ 200 nm, respectively. For

13   the $SnO_2$-Cu-10h (Fig. 1d and Fig. S1), the $SnO_2$ nanoparticles of 30 ~ 200 nm (white dots)

14   are homogeneously distributed in the continuous Cu matrix (grey region), which experiences

15   considerable agglomeration due to the drastic cold welding by mechanical impact of steel

16   balls. As the milling time increases to 50h (Fig.1e), the disappearance of $SnO_2$ particles

17   indicates the further grain refinement of $SnO_2$ and fully embedding of $SnO_2$ in the continuous

18   Cu matrix.

19      To further investigate the distribution of $SnO_2$ in Cu matrix, the $SnO_2$-Cu-50h sample is

20   characterized by TEM, and the results are shown in Fig. 1f-h. The bright-field TEM image

21   (Fig. 1f) combined with the selected-area electron diffraction patterns (Fig. 1g) indicate the

1  homogeneous microstructure of $SnO_2$-Cu composite, while the high resolution TEM image

2  (Fig. 1h) identifies the Cu and $SnO_2$ phases according to their characteristic planar distances.

3  The measured Cu(111) inter-planar distance of 0.213 nm is slightly larger than the standard

4  value (0.208 nm, JCPDS No. 03-065-9743) because of the formation of Cu(Sn) solid solution,

5  which also agrees well with the XRD result (Fig. 1a). Importantly, it is clearly seen from Fig.

6  1h that the grain size of $SnO_2$ and Cu crystals are both about 10 nm, and the nanosized $SnO_2$

7  are homogeneously embedded in the nanocrystalline Cu matrix. The nanocrystalline structure

8  of Cu matrix is formed due to the repeated cold welding and fracturing in the milling

9  process.[27-29]

10  Fig. 2a shows the initial discharge-charge profiles of the $SnO_2$-Cu-0h, $SnO_2$-Cu-10h,

11  $SnO_2$-Cu-50h composite electrodes at a current density of 85 mA $g^{-1}$. The initial discharge and

12  charge capacities of the $SnO_2$-Cu-0h, $SnO_2$-Cu-10h, $SnO_2$-Cu-50h electrodes are 716.4 and

13  231.2 mAh $g^{-1}$, 770.8 and 500.9 mAh $g^{-1}$, 752.4 and 566.5 mAh $g^{-1}$ respectively,

14  corresponding to the ICE of 32.3%, 65.0%, 75.3% respectively. It is noted that the initial

15  discharge capacity of $SnO_2$-Cu-50h is close to its theoretical value (1494 x 54.25% = 810.5

16  mAh $g^{-1}$) if only considering the contribution of the $SnO_2$ component in the $SnO_2$-Cu

17  composite. To give a more accurate comparison of ICE between different $SnO_2$-Cu composite

18  electrodes, the ICE statistics from six cells and the ICE values (mean ± standard deviation) for

19  the $SnO_2$-Cu-0h, $SnO_2$-Cu-10h, $SnO_2$-Cu-50h composites are listed in Table 1. It is shown

20  that the $SnO_2$-Cu-50h electrode has the highest ICE of 76.0±1.5%, which is much higher than

21  the theoretical value 52.4% and those for the $SnO_2$-Cu-10h electrode (66.3±1.4%) and the

1    SnO$_2$-Cu-0h electrode (30.9±1.7%). This result is also much higher than previously reported

2    ICE values of SnO$_2$ based anodes.[21-24, 30-33] Obviously, both the ICE and the initial reversible

3    capacity increase with the milling time, which implies the improved reversibility of SnO$_2$.

4          The role of Cu additive is further confirmed by comparing the long-term Coulombic

5    efficiency of the SnO$_2$-Cu-50h and SnO$_2$-50h electrodes. As shown in Fig. 2b, although the

6    SnO$_2$-50h electrode shows high ICE of 74.4±1.9% (Table 1), its CE increases gradually up to

7    94.1% at the 15$^{th}$ cycle. Comparatively, the CE of SnO$_2$-Cu-50h electrode rapidly increases up

8    to 95.6% at the second cycle and almost keeps stable in the subsequent cycles.

9          To understand the improvement in the Coulombic efficiency, the reaction mechanism of

10   SnO$_2$ is investigated by CV analysis on the SnO$_2$-Cu-0h, SnO$_2$-50h and SnO$_2$-Cu-50h

11   electrodes. Fig. 3 compares the initial five CV curves of these three electrodes. Two cathodic

12   peaks *B*, *C* and an anodic peak *C′* appear in the first cycle for all three electrodes, which are

13   respectively attributed to the reduction of SnO$_2$ to metallic Sn, the alloying of Li with Sn to

14   form Li$_x$Sn during lithiation, and the Li$_x$Sn de-alloyed into metallic Sn during delithiation. For

15   the SnO$_2$-Cu-50h electrode (Fig. 3a), the characteristic peak *B* shows good reproducibility in

16   the subsequent cycles, indicating the reversible formation of SnO$_2$ from the redox reaction of

17   Li$_2$O in the charging process, which is also verified by two broad anodic peaks above 1.3V. To

18   be specific, the anodic peak *B$_1$′* at ca. 1.35V should be attributed to the redox reaction

19   between Sn and Li$_2$O to form SnO (Sn + Li$_2$O $\rightarrow$ SnO + 2Li$^+$ +2e$^-$), while the anodic peak *B$_2$′*

20   at ca. 1.80V should be ascribed to the further redox reaction between SnO and Li$_2$O to

21   regenerate SnO$_2$ (SnO + Li$_2$O $\rightarrow$ SnO$_2$ + 2Li$^+$ + 2e$^-$), which is in agreement with the previous

1    CV results on the reversible formation of $SnO_2$.[7-11] In addition, it is noted that there is no

2    anodic peak of the redox reaction of $Li_2O$ with Cu for these three electrodes, which should

3    appear above 2.5V.[34, 35] These results demonstrate that the Cu additive is electrochemically

4    inactive to react with $Li_2O$, but it promotes the reversible formation of $SnO_2$.

5        Comparatively, Fig. 3b shows no characteristics of redox reaction of $Li_2O$ even at the first

6    cycle, which explains the rather low ICE for the $SnO_2$-Cu-0h electrode. With respect to the

7    $SnO_2$-50h electrode (Fig. 3c), the anodic peaks $B_1'$, $B_2'$ becomes rapid weakening with the

8    cycling number, similar situation also occurs on the cathodic peak $B$, indicating the declined

9    reversibility of $SnO_2$ in the $SnO_2$-50h electrode. This comparison among the CV results of

10   $SnO_2$-Cu-0h, $SnO_2$-Cu-50h, $SnO_2$-50h electrodes clearly indicates that nanosized $SnO_2$ and

11   the surrounding Cu nanocrystalline structure are beneficial to the reversible formation of

12   $SnO_2$ from $Li_2O$ and Sn, as previously reported for the Ni-$Co_3O_4$ anode.[25]

13       Unfortunately, the $SnO_2$-Cu-50h electrode shows rapid capacity fade during cycling, as

14   shown in Fig. 2b, where the cycling performance of $SnO_2$-50h is also compared. The charge

15   capacity of the $SnO_2$-Cu-50h electrode decreases from 566.5 mAh $g^{-1}$ to 94.8 mAh $g^{-1}$ after 55

16   cycles, with the capacity retention ratio of only 16.7%. Comparatively, the $SnO_2$-Cu-50h

17   electrode has better cyclic stability than the $SnO_2$-50h electrode, but relatively lower initial

18   charge capacity, which is due to higher theoretical capacity (1494 mAh $g^{-1}$) for the $SnO_2$-50h

19   electrode. The poor cyclic performance for the $SnO_2$-Cu composite electrode should be

20   mainly due to the large volume variation during cycling, which causes the cracking and

21   pulverization of microsized Cu matrix embedded with $SnO_2$ nanoparticles, finally leading to

1 the disconnection of active particles from the current collector. Therefore, to achieve better

2 cyclic performance, the $SnO_2$-Cu composite is further milled with graphite to obtain

3 $SnO_2$-Cu-C multiphase composite.

4 **3.2 $SnO_2$-Cu-C composites**

5 The cyclic performance of $SnO_2$-Cu-C composites with different amount of graphite and

6 $SnO_2$-C composite are shown in Fig. 4a. The $SnO_2$-Cu-50h-10%C, $SnO_2$-Cu-50h-20%C,

7 $SnO_2$-Cu-50h-30%C and $SnO_2$-50h-30%C composites have the theoretical capacity range of

8 419.0~766.6, 413.8~722.8, 408.5~678.9 and 659~1157.4 mAh $g^{-1}$, respectively. The former

9 value in each composites based on the theoretical capacity of alloying/de-alloying reaction

10 (782 mAh $g^{-1}$) of $SnO_2$, while the latter value is based on the theoretical capacity of both

11 alloying/de-alloying and conversion reactions (1494 mAh $g^{-1}$) of $SnO_2$, the detailed

12 calculation process is based on the method in Ref. [36] and shown in the ESI. As shown in Fig.

13 4a, the $SnO_2$-Cu-50h-10%C, $SnO_2$-Cu-50h-20%C, $SnO_2$-Cu-50h-30%C electrodes deliver the

14 initial charge capacity of 753.3, 681.7, 605.8 mAh $g^{-1}$ at the current density of 100 mA $g^{-1}$,

15 which retain 124.8, 306.5, 450.8 mAh $g^{-1}$ at $80^{th}$ cycle, corresponding to the capacity retention

16 ratio of 16.6%, 45.0%, 74.4%, respectively. On one side, as the graphite ratio increased from

17 10 wt. % to 30 wt. %, the initial charge capacity of the corresponding $SnO_2$-Cu-C composite

18 decreased because of the reduced theoretical capacity. On the other side, it clearly

19 demonstrates that the sufficient addition of graphite greatly improves the cyclic stability of

20 $SnO_2$-Cu-C composite.

21 Fig. 4a further compares the cyclic performance of the $SnO_2$-Cu-50h-30%C electrode

1   with the $SnO_2$-Cu-10h-30%C and $SnO_2$-50h-30%C electrodes, which exhibit the initial charge

2   capacity of 657.6, 807.9 mAh $g^{-1}$, and retain 258.2, 76.7 mAh $g^{-1}$ at the 80th cycle, with the

3   capacity retention ratio being 39.3% and 9.5%, respectively. Apparently, the capacity

4   retention of the $SnO_2$-Cu-50h-30%C electrode (74.4%) is much higher than those of the

5   $SnO_2$-Cu-10h-30%C and $SnO_2$-50h-30%C electrodes, indicating the positive effect of

6   nanocrystalline Cu matrix on the cyclic stability of $SnO_2$. In addition, the $SnO_2$-Cu-50h-30%C

7   electrode shows the ICE of 79.1±2.1% (Table 1), implying the maintenance of the high

8   reversibility of $Li_2O$ after further milling with graphite, its reversible anodic peaks of Sn, SnO

9   with $Li_2O$ are also verified in the CV curves as shown in Fig.3d. Furthermore, the specific

10  capacity and cycleability of present $SnO_2$-Cu-50h-30%C composite are better than previously

11  reported $SnO_2$-based composite anodes.[22-24, 32]

12      As the $SnO_2$-Cu-50h-30%C composite has superior cyclic performance to other

13  $SnO_2$-Cu-C composites, its rate capability is further investigated, and the result is shown in

14  Fig. 4b. The $SnO_2$-Cu-50h-30%C electrode maintains a stable reversible capacity of about

15  335.0 mAh $g^{-1}$ at a high current density of 1.0 A $g^{-1}$, and a charge capacity of about 560.0

16  mAh $g^{-1}$ could be restored as the current density is back to 0.1 A $g^{-1}$. This result indicates the

17  excellent rate performance for the $SnO_2$-Cu-50h-30%C composite electrode.

18      The enhanced electrochemical performances of the $SnO_2$-Cu-50h-30%C electrode are

19  related to its carbon-matrix composite structure, as shown in the SEM image of Fig. 5a, and

20  the back-scattered electron SEM image of Fig. S2 (see the ESI). It is clearly seen that the

21  $SnO_2$-Cu particles of different particle size (50~500 nm) are embedded in the graphite layers,

1    forming the dual scale embedding structure in the $SnO_2$-Cu-50h-30%C composite. That is to

2    say, the $SnO_2$ nanoparticles are embedded in nanocrystalline Cu matrix, meanwhile the

3    $SnO_2$-Cu composite particles are embedded in microsized graphite matrix. The dual scale

4    embedding structure is schematically shown in Fig. 5b, in which the role of the Cu and

5    graphite additives on the electrochemical performances of $SnO_2$ are discussed as follows:

6          Firstly, in the aspect of electrical conductivity, both Cu and graphite act as good

7    conductive media for electron transport, which is quite important for the redox reaction of the

8    insulating oxide $Li_2O$. On one hand, the Cu nanocrystals surrounding the active $SnO_2$

9    nanoparticles allow the fast electron transport inside the $SnO_2$-Cu particles. On the other hand,

10   the microsized graphite sheets construct a soft three-dimensional conductive network to

11   bridge all of $SnO_2$-Cu particles, ensuring good electrical conductivity even the $SnO_2$-Cu

12   particles are cracked and pulverized during cycling. Secondly, with respect to the

13   enhancement of cyclic stability, the most important reason is that the three dimensional

14   network of microsized graphite sheets could effectively buffer the volume change of Li

15   insertion/extraction in the $SnO_2$-Cu composite embedded in the graphite matrix. It also avoids

16   the disconnection of active $SnO_2$-Cu particles with the collector, and maintains the electrode

17   integrity. Furthermore, the nanocrystalline Cu matrix could hinder the aggregation of

18   nanosized $SnO_2$ and Sn particles, and maintain the nanostructure during cycling. All of these

19   aspects are beneficial to reduce the loss of the active $SnO_2$ or Sn, and thus preserve the

20   reversible capacity fade of the composite electrode. In summary, the overall enhancements in

21   the conductivity of electron and the nanostructure stability due to dual scale embedding

1 structure of nanosized Cu and microsized graphite matrix are responsible for the greatly

2 improved ICE and cycleability in the $SnO_2$-Cu-C composite anode.

3

4 **4. Conclusions**

5 The $SnO_2$-Cu and $SnO_2$-Cu-C composite anodes with improved ICE and cyclic stability

6 have been produced by ball milling. For the $SnO_2$-Cu composite, the nanocrystalline Cu

7 matrix and the resultant good electrical conductivity promoted the reversibility of nanoscale

8 $SnO_2$ from $Li_2O$ and Sn. The 50h-milled $SnO_2$-Cu composite electrode showed a high ICE of

9 76.0±1.5% at 85 mA $g^{-1}$, much higher than the theoretical value of 52.4% when the

10 conversion reaction was irreversible. The further milling of $SnO_2$-Cu with graphite leaded to

11 dual scale embedding structure, namely that nanosized $SnO_2$ were embedded in

12 nanocrystalline Cu matrix, while the $SnO_2$-Cu composite particles were embedded in

13 microsized graphite matrix. As a result, the $SnO_2$-Cu-50h-30%C composite delivered a higher

14 ICE of 79.1±2.1%, and reversible charge capacity of 450.8 mAh $g^{-1}$ after 80 cycles at 100 mA

15 $g^{-1}$, with the capacity retention ratio of 74.4%. This unique multiphase structure could be

16 further optimized in the composition and adopted to other high-capacity anode materials.

17

18 **Acknowledgments**

3

4    **References**

5    1.   J. B. Goodenough and Y. Kim, *Chem. Mat.*, 2010, **22**, 587-603.

6    2.   V. Etacheri, R. Marom, R. Elazari, G. Salitra and D. Aurbach, *Energy Environ. Sci.*,

7      2011, **4**, 3243-3262.

8    3.   M. Armand and J. M. Tarascon, *Nature*, 2008, **451**, 652-657.

9    4.   Y. Idota, T. Kubota, A. Matsufuji, Y. Maekawa and T. Miyasaka, *Science*, 1997, **276**,

10      1395-1397.

11    5.   M. V. Reddy, G. V. Subba Rao and B. V. R. Chowdari, *Chem. Rev.*, 2013, **113**,

12      5364-5457.

13    6.   N. C. Li and C. R. Martin, *J. Electrochem. Soc.*, 2001, **148**, A164-A170.

14    7.   V. Aravindan, K. B. Jinesh, R. R. Prabhakar, V. S. Kale and S. Madhavi, *Nano Energy*,

15      2013, **2**, 720-725.

16    8.   V. Aravindan, J. Sundaramurthy, E. N. Kumar, P. S. Kumar, W. C. Ling, R. V. Hagen, S.

17      Mathur, S. Ramakrishna and S. Madhavi, *Electrochim. Acta*, 2014, **121**, 109-115.

18    9.   S. T. Chang, I. C. Leu, C. L. Liao, J. H. Yen and M. H. Hon, *J. Mater. Chem.*, 2004, **14**,

19      1821-1826.

20    10.   F. Han, W. C. Li, M. R. Li and A. H. Lu, *J. Mater. Chem.*, 2012, **22**, 9645-9651.

21    11.   W. Xu, N. L. Canfield, D. Wang, J. Xiao, Z. Nie and J. G. Zhang, *J. Power Sources*,

1      2010, **195**, 7403-7408.

2    12.   X. W. Guo, X. P. Fang, Y. Sun, L. Y. Shen, Z. X. Wang and L. Q. Chen, *J. Power*

3      *Sources*, 2013, **226**, 75-81.

4    13.   A. Nie, L. Y. Gan, Y. Cheng, H. Asayesh Ardakani, Q. Li, C. Dong, R. Tao, F.

5      Mashayek, H. T. Wang, U. Schwingenschloegl, R. F. Klie and R. S. Yassar, *Acs Nano*,

6      2013, **7**, 6203-6211.

7    14.   I. A. Courtney and J. R. Dahn, *J. Electrochem. Soc.*, 1997, **144**, 2045-2052.

8    15.   J. Y. Huang, L. Zhong, C. M. Wang, J. P. Sullivan, W. Xu, L. Q. Zhang, S. X. Mao, N. S.

9      Hudak, X. H. Liu, A. Subramanian, H. Fan, L. Qi, A. Kushima and J. Li, *Science*, 2010,

10      **330**, 1515-1520.

11    16.   Y. Wang, H. C. Zeng and J. Y. Lee, *Adv. Mater.*, 2006, **18**, 645-649.

12    17.   W. M. Zhang, J. S. Hu, Y. G. Guo, S. F. Zheng, L. S. Zhong, W. G. Song and L. J. Wan,

13      *Adv. Mater.*, 2008, **20**, 1160-1165.

14    18.   S. Ding, D. Luan, F. Y. C. Boey, J. S. Chen and X. W. Lou, *Chem. Commun.*, 2011, **47**,

15      7155-7157.

16    19.   X. W. Lou, D. Deng, J. Y. Lee and L. A. Archer, *Chem. Mat.*, 2008, **20**, 6562-6566.

17    20.   L. Yuan, K. Konstantinov, G. X. Wang, H. K. Liu and S. X. Dou, *J. Power Sources*,

18      2005, **146**, 180-184.

19    21.   H. Liu, R. Hu, M. Zeng, J. Liu and M. Zhu, *J. Mater. Chem.*, 2012, **22**, 8022-8028.

20    22.   H. Liu, R. Hu, W. Sun, M. Zeng, J. Liu, L. Yang and M. Zhu, *J. Power Sources*, 2013,

21      **242**, 114-121.

1   23.  D. W. Jung, J. H. Jeong, B. C. Cha, J. B. Kim, B. S. Kong, J. K. Lee and E. S. Oh, *Met.*

2         *Mater. Int.*, 2011, **17**, 1021-1026.

3   24.  F. Belliard and J. Irvine, *J. Power Sources*, 2001, **97**, 219-222.

4   25.  Y. M. Kang, K. T. Kim, J. H. Kim, H. S. Kim, P. S. Lee, J. Y. Lee, H. K. Liu and S. X.

5         Dou, *J. Power Sources*, 2004, **133**, 252-259.

6   26.  K. Fukuda, K. Kikuya, K. Isono and M. Yoshio, *J. Power Sources*, 1997, **69**, 165-168.

7   27.  C. Suryanarayana, *Prog. Mater. Sci.*, 2001, **46**, 1-184.

8   28.  H. J. Fecht, E. Hellstern, Z. Fu and W. L. Johnson, *Metall. Mater. Trans. A*, 1990, **21A**,

9         2333-2337.

10  29.  C. Suryanarayana and F. H. Froes, *Metall. Mater. Trans. A*, 1992, **23A**, 1071-1081.

11  30.  L. Li, X. Yin, S. Liu, Y. Wang, L. Chen and T. Wang, *Electrochem. Commun.*, 2010, **12**,

12        1383-1386.

13  31.  C. H. Yim, E. A. Baranova, F. M. Courtel, Y. Abu Lebdeh and I. J. Davidson, *J. Power*

14        *Sources*, 2011, **196**, 9731-9736.

15  32.  M. S. Park, G. X. Wang, Y. M. Kang, D. Wexler, S. X. Dou and H. K. Liu, *Angew.*

16        *Chem. Int. Ed.*, 2007, **46**, 750-753.

17  33.  R. Demir Cakan, Y. S. Hu, M. Antonietti, J. Maier and M. M. Titirici, *Chem. Mat.*, 2008,

18        **20**, 1227-1229.

19  34.  X. H. Huang, C. B. Wang, S. Y. Zhang and F. Zhou, *Electrochim. Acta*, 2011, **56**,

20        6752-6756.

21  35.  X. P. Gao, J. L. Bao, G. L. Pan, H. Y. Zhu, P. X. Huang, F. Wu and D. Y. Song, *J. Phys.*

1        *Chem. B*, 2004, **108**, 5547-5551.

2    36.    N. R. Srinivasan, S. Mitra and R. Bandyopadhyaya, *Phys. Chem. Chem. Phys.*, 2014, **16**,

3            6630-6640.

4

5

6

7

8

9

10

11

12

13

14

15

16

17

18

19

20

21

22

23

24

25

26

27

28

1

2

3

4　**Table**

5　　**Table 1.** The statistics, mean (μ) and standard deviation (σ) of ICE for different composite electrodes

| ICE(%) Sample / Electrode | 1 | 2 | 3 | 4 | 5 | 6 | μ±σ |
|---|---|---|---|---|---|---|---|
| SnO$_2$-Cu-0h | 28.2 | 30.0 | 30.7 | 31.2 | 32.3 | 32.8 | 30.9±1.7 |
| SnO$_2$-Cu-10h | 64.8 | 65.2 | 65.6 | 66.2 | 67.7 | 68.3 | 66.3±1.4 |
| SnO$_2$-Cu-50h | 73.8 | 74.8 | 75.3 | 76.8 | 77.4 | 77.6 | 76.0±1.5 |
| SnO$_2$-50h | 72.1 | 72.8 | 73.8 | 74.6 | 76.4 | 76.7 | 74.4±1.9 |
| SnO$_2$-Cu-50h-30%C | 76.7 | 77.3 | 78.2 | 79.3 | 80.6 | 82.3 | 79.1±2.1 |

6

7

8

9

10

11

12

13

14

15

16

17

18

19

20

21

22

1    **Figures**
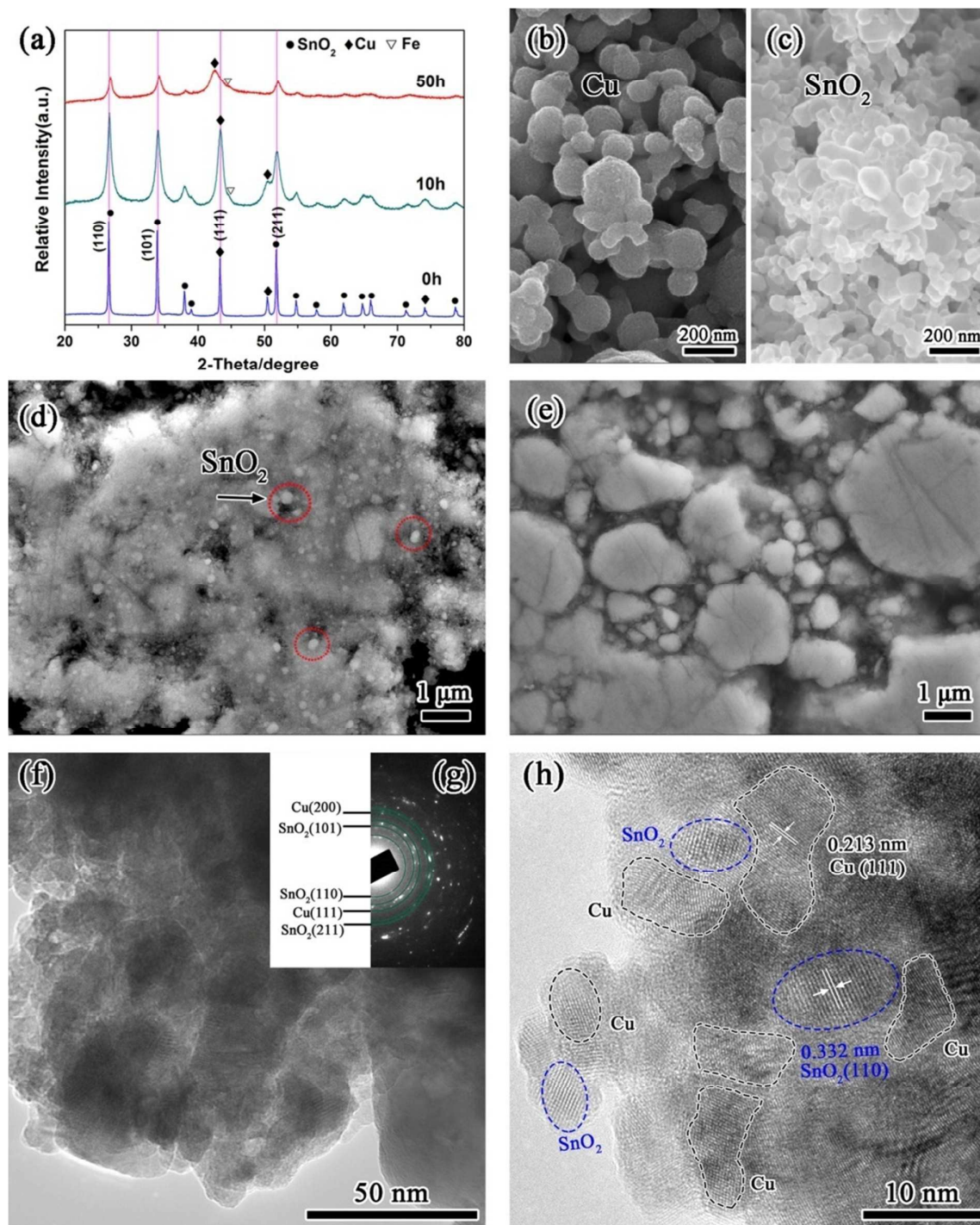


2

3    **Fig. 1** (a) XRD patterns of $SnO_2$-Cu-0h, $SnO_2$-Cu-10h, $SnO_2$-Cu-50h composites; SEM micrographs of raw

4        materials and $SnO_2$-Cu composites for different milling time: (b) pristine Cu, (c) pristine $SnO_2$, (d)

5    $SnO_2$-Cu-10h, (e) $SnO_2$-Cu-50h; (f) Bright-field TEM image, (g) selected electron diffraction pattern (inset

at the top right), and (h) high-resolution TEM image of the $SnO_2$-Cu-50h composite.
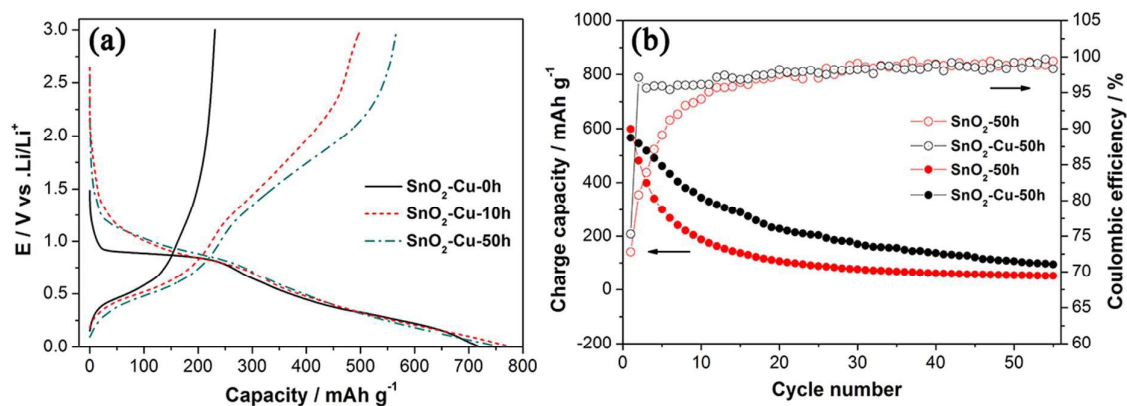


**Fig. 2** (a) Initial discharge-charge profiles of $SnO_2$-Cu-0h, $SnO_2$-Cu-10h, and $SnO_2$-Cu-50h electrodes

between 0.01 and 3.0 V *vs.* $Li^+$/Li at 85 mA $g^{-1}$; (b) Comparative cycling performance for the $SnO_2$-Cu-50h

and $SnO_2$-50h electrodes from 0.01V to 3.0V *vs* .Li/$Li^+$ at 85 mA $g^{-1}$.
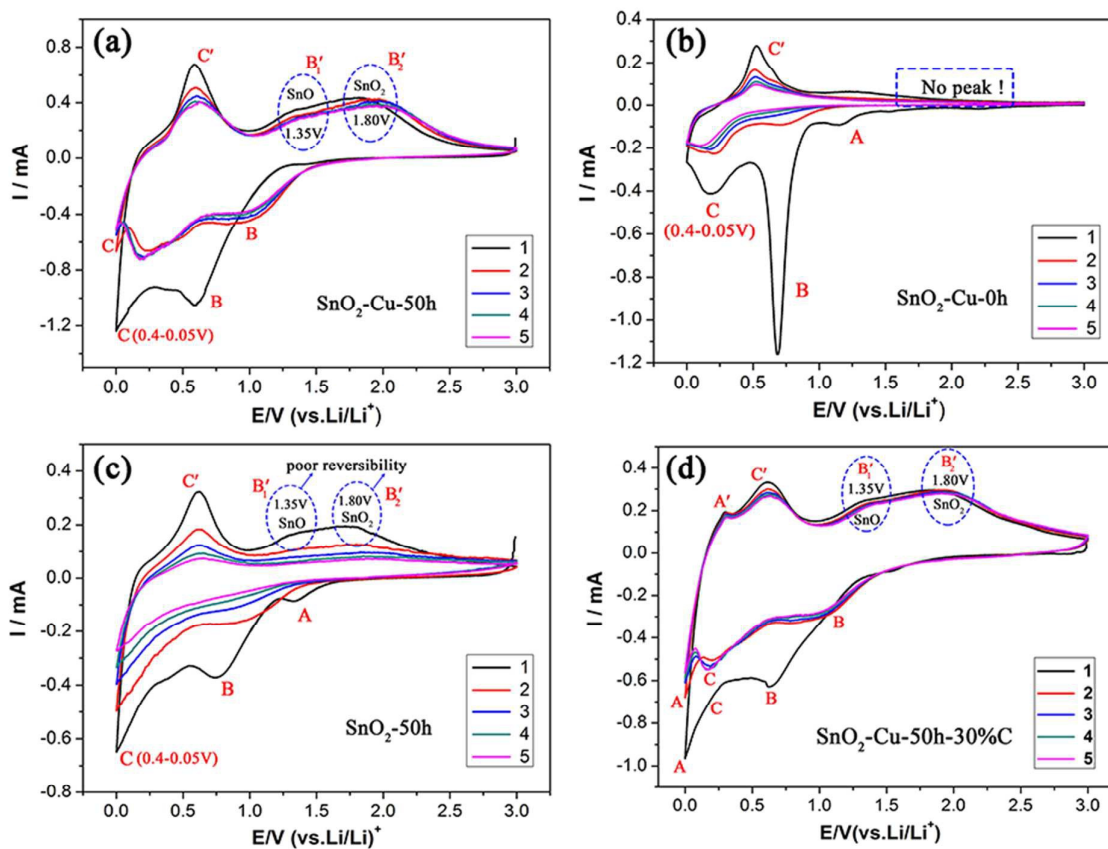
**Fig. 3** CV curves for (a) SnO$_2$-Cu-50h, (b) SnO$_2$-Cu-0h, (c) SnO$_2$-50h and (d) SnO$_2$-Cu-50h-30%C

electrodes in the potential range of 0.0V−3.0V *vs*. Li$^+$/Li at scanning rate of 0.2 mv s$^{-1}$.

1

2

3

4

5

6

7

8

9

10

11
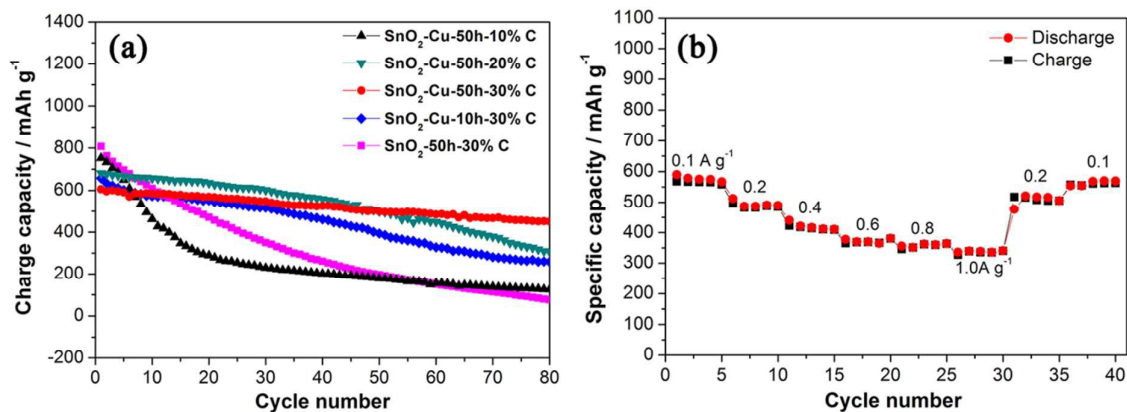
**Fig. 4** (a) Comparison of cyclic performance for the $SnO_2$-Cu-50h-10%C, $SnO_2$-Cu-50h-20%C, $SnO_2$-Cu-50h-30%C, $SnO_2$-Cu-10h-30%C and $SnO_2$-50h-30%C composites between 0.01 and 3.0 V *vs*. $Li^+$/Li at 100 mA $g^{-1}$; (b) Rate capability of $SnO_2$-Cu-50h-30%C electrode with a current density range from 0.1 A $g^{-1}$ to 1.0 A $g^{-1}$, cut off potential :0.01−3V *vs*. $Li^+$/Li.
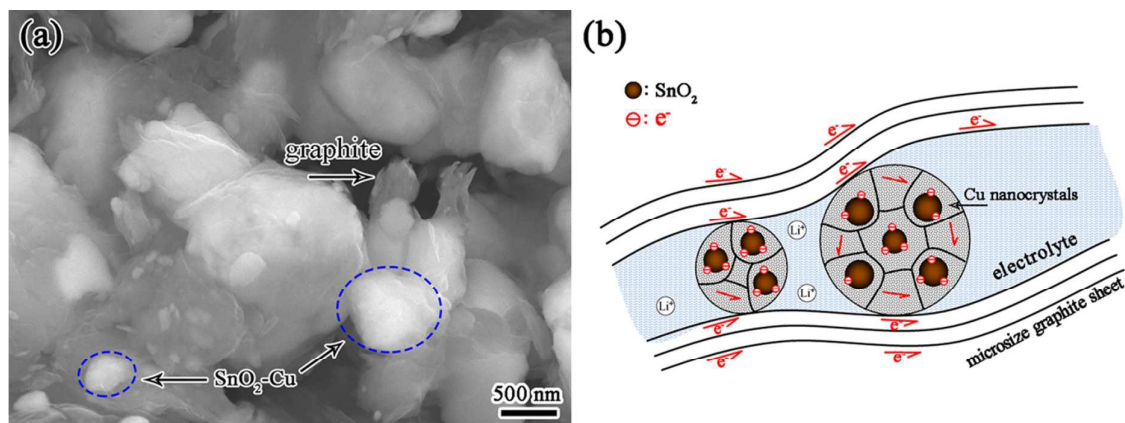
**Fig. 5** (a) SEM image of the $SnO_2$-Cu-50h-30%C composite; (b) Schematic diagram of dual scale embedding structure showing the enhanced electron transportation and lithium ion diffusion in the $SnO_2$-Cu-C composite.